PAPER

Highly anisotropic thermoelectric properties of black phosphorus crystals

To cite this article: Qingsheng Zeng *et al* 2019 *2D Mater.* **6** 045009

2D Materials

RECEIVED
1 April 2019

REVISED
4 June 2019

ACCEPTED FOR PUBLICATION
10 June 2019

PUBLISHED
8 July 2019

PAPER

Highly anisotropic thermoelectric properties of black phosphorus crystals

Qingsheng Zeng[1,10], Bo Sun[2,10], Kezhao Du[3], Weiyun Zhao[1], Peng Yu[4], Chao Zhu[1], Juan Xia[5], Yu Chen[1], Xun Cao[1], Qingyu Yan[1], Zexiang Shen[6], Ting Yu[6], Yi Long[1], Yee Kan Koh[7,8] and Zheng Liu[1,9]

[1] School of Materials Science and Engineering, Nanyang Technological University, Singapore
[2] Tsinghua-Berkeley Shenzhen Institute and Guangdong Provincial Key Laboratory of Thermal Management Engineering and Materials, TSIGS, Tsinghua University, Shenzhen, People's Republic of China
[3] College of Chemistry and Materials Science, Fujian Provincial Key Laboratory of Advanced Materials Oriented Chemical Engineering, Fujian Normal University, Fuzhou, People's Republic of China
[4] School of Materials Science and Engineering, Sun Yat-sen University, Guangzhou, People's Republic of China
[5] Institute of Fundamental and Frontier Sciences, University of Electronic Science and Technology of China, Chengdu, People's Republic of China
[6] Division of Physics and Applied Physics, School of Physical and Mathematical Sciences, Nanyang Technological University, Singapore
[7] Department of Mechanical Engineering, National University of Singapore, Singapore
[8] Centre for Advanced 2D Materials, National University of Singapore, Singapore
[9] CINTRA CNRS/NTU/THALES, UMI 3288, Research Techno Plaza, Singapore
[10] These authors contributed equally to this work.

E-mail: mpekyk@nus.edu.sg **and** z.liu@ntu.edu.sg

Keywords: black phosphorus, thermoelectric property, anisotropy, 2D material

Supplementary material for this article is available online

Abstract

Black phosphorus captures enormous research attention on the anisotropic properties due to its orthorhombic crystal structure. Here the in-plane anisotropic thermoelectric behaviors of bulk black phosphorus crystals in the temperature range from 300 K to 600 K are reported for the first time. Based on the home-grown big size and high-quality black phosphorus crystals, the electrical conductivity and Seebeck coefficient are simultaneously measured by a ZEM-3 instrument system, and the thermal conductivity is measured by time-domain thermoreflectance (TDTR). For each individual parameter, the values along the zigzag and armchair directions show the same temperature-dependent trend. However, the electrical conductivity along the armchair direction is ~ two times of that along the zigzag direction, while the thermal conductivity along the armchair direction is only ~ one third of that along the zigzag direction. Furthermore, the Seebeck coefficients show almost isotropic behavior. As a result, the figure of merit *ZT* along the armchair direction is as large as ~5.5 times of that along the zigzag direction, exhibiting high anisotropy. The results of intrinsic, orientation-dependent thermoelectric behaviors not only shed light on the fundamental physical properties of black phosphorus but also provide guidelines in the device design for potential thermoelectric applications.

Introduction

Black phosphorus (BP) is a prototypical single-element two-dimensional (2D) semiconductor with high carrier mobility [1–3] and a thickness-dependent direct bandgap tunable from 1.5–1.7 eV for monolayer to 0.3–0.35 eV for bulk [4–6]. Its orthorhombic crystal structure leads to remarkable in-plane anisotropy, which distinguishes BP from many other 2D materials. As shown in figures 1(a)–(c), each phosphorus atom is covalently bonded with three adjacent atoms to form layers with a puckered honeycomb structure, and the layers are stacked together by van der Waals interactions, resulting in three orthogonal principle axes of zigzag (ZZ), armchair (AC) and through-plane (TP) [7]. This structure inspires enormous interest in the anisotropy study of various properties, such as electronic [1, 5], optical [6, 8–12], thermal [13–19], vibrational [20–24], mechanical [25–27] and optoelectronic properties [8, 28–30]. BP has also been theoretically predicted to be a unique thermoelectric material with an interesting opposite in-plane

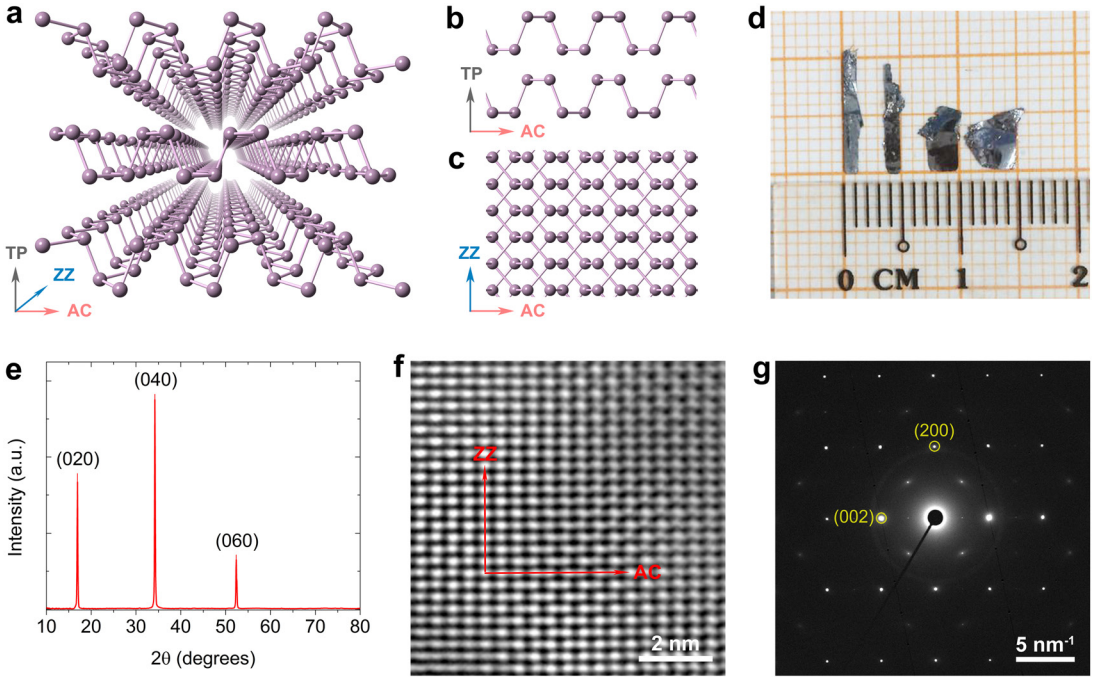

Figure 1. Crystal structure and characterization of BP crystals. (a) Perspective, (b) side and (c) top view of few-layer phosphorene. (d) Optical image of isolated BP crystals. AC, ZZ and TP denote armchair, zigzag and through-plane direction respectively. (e) Powder XRD pattern of BP flakes. (f) High-resolution TEM lattice image of a BP flake. (g) Selected area electron diffraction pattern taken from the area shown in (f).

anisotropy in electrical and thermal conductivities, that is a higher electrical conductivity along the AC direction while a higher thermal conductivity along the ZZ direction [31, 32]. However, systematically experimental investigation of the anisotropic thermoelectric properties is still in demand.

The thermoelectric efficiency is determined by the dimensionless figure of merit $ZT = (S^2\sigma/\Lambda)T$, which is derived from a combination of three parameters except for the absolute temperature T: the electrical conductivity σ, the thermal conductivity Λ, and the Seebeck coefficient S. To date, the full picture of the anisotropic thermoelectric performances is still lacking because most of works just focused on one or two parameters and failed to cover the high-temperature range. There are only two reports about the anisotropic electrical conductivity of BP, which exhibit the temperature-dependent behaviors (from room temperature to 2 K) for bulk crystals [1, 19]. The reported electrical conductivity has a low value of <10 S cm^{-1} in both the AC and ZZ directions at room temperature, and a high ratio of ~3.5 between the two directions, which is almost twice of the value (1.5–2.1) obtained from the angle-resolved DC conductance measurement on the exfoliated flakes [3, 5, 20]. The anisotropic thermal conductivity of BP flakes has been measured by micro-Raman spectroscopy [13], micro-bridge technique [14, 17], time-domain thermoreflectance (TDTR) [15, 18], and time-resolved magneto-optical Kerr effect [16]. The results near room temperature derived from the flakes with different thickness show large deviations. The thermal conductivity is 5–20 W m^{-1} K^{-1} along the AC direction and 12–40 W m^{-1} K^{-1} along the ZZ direction for the flakes ranging from 9 to 300 nm [13, 14], and these values increase to 26–36 W m^{-1} K^{-1} and 80–101 W m^{-1} K^{-1} respectively as the crystal thickness increases to 500 nm–300 μm [15, 16, 18]. Although the deviations may partially originate from the different measurement methods, and the ultra-low thermal conductivity for thin flakes are presumably caused by the surface contamination and oxidation, the thickness dependence has been clearly demonstrated via the thermal conductivity measurement along the AC direction on the BP flakes with a thickness of 40–270 nm [17]. The thermal conductivity and Seebeck coefficient of BP crystals along the three principle directions were simultaneously measured by Physical Property Measurement System between 10 and 300 K [33]. However, both the obtained thermal conductivities and the bandgap (0.17 eV) extracted from the maximum of Seebeck coefficient are significantly lower than the ones in other reports. The room temperature ZT values along the AC and ZZ directions were obtained from nanoribbons with the thickness of 170 nm and 200 nm respectively [14], but the results with low values are probably not reliable due to the degradation of BP flakes during the sample preparation process. It can be seen that the bulk crystal is more suitable for evaluating the intrinsic thermoelectric performances of BP to avoid the uncertainty caused by the thickness or by the degradation of the sample. On the other hand, the studies of thermoelectrics usually aim at high-temperature domain. BP bulk crystals are much more thermostable than flakes with

a sublimation temperature of around 770 K [34, 35], making it is possible for BP to study the high-temperature thermoelectric properties like the common thermoelectric materials. To investigate the anisotropic thermoelectric properties of bulk BP, two main prerequisites should be needed: one is the synthesis of large-size and high-quality BP crystals and the other is the reliable and accurate experimental techniques.

Herein, we study the in-plane anisotropic thermoelectric behaviors of BP bulk crystals between 300 and 600 K, which is the first time to systematically investigate all the thermoelectric variables for BP in a wide temperature range. To achieve this objective, we synthesize high-quality and big-size BP crystals with regular shape, and employ the reliable ZEM-3 system to measure the electrical conductivity and Seebeck coefficient simultaneously. Additionally, we are experienced with accurate measurements of in-plane [36] and through-plane [37] thermal conductivity by TDTR, and succeeded in the anisotropic thermal measurement of BP below 300 K [18], which are extended up to 600 K in this work. The obtained electrical conductivity and thermal conductivity demonstrate obvious anisotropy between the AC and ZZ directions, while the Seebeck coefficient shows almost isotropic behavior. Therefore, the resulting *ZT* shows large anisotropy over the whole temperature range.

Results and discussions

BP synthesis and characterization

BP bulk crystals were synthesized using a chemical vapor transport method [38], through a short way transport of red phosphorus from hot zone to cold zone with Sn/SnI_4 as the mineralization additive. In a typical growth process, 500 mg red phosphorus, 20 mg Sn and 10 mg SnI_4 were mixed and loaded in a quartz ampoule of 10 cm in length and 1.0 cm in diameter. The ampoule was evacuated to a low pressure of $\sim 1 \times 10^{-5}$ Torr and placed horizontally in a two-zone tube furnace, with the starting material located in the hot zone and the empty end in the colder zone. The critical approaches to grow large BP crystals are the small temperature difference between the two zones and the slow crystallization rate. In our optimized process, the furnace was set to be 650 °C and 600 °C for the hot zone and the colder zone respectively with a ramp time of 3 h and kept at this temperature for 2 h. Then, the ampoule was slowly cooled down to 300 °C in 100 hrs, followed by naturally cooled down to room temperature.

As shown in figure S1(a) (stacks.iop.org/TDM/6/045009/mmedia), shiny BP ribbon crystals nucleated together as a bundle in the colder end of the ampoule. The longer side of the BP ribbon crystal is along the ZZ direction, whose size can be larger than 10 mm. Compared to previous reports [39, 40], the important improvement of our crystals lies in the much larger size in the AC direction, which can approach 5 mm (figure 1(d)) due to the slow growth process. In the TP direction, the thickness of our samples is distributed between 100 and 200 μm. The as-grown large-size crystals provide the possibility to study the anisotropic properties.

In order to investigate the intrinsic properties, the top layers of BP crystals are exfoliated to expose the fresh surface before all the characterization and the following thermoelectric measurements. Powder x-ray diffraction (XRD) confirms the pure BP phase with orthorhombic (Cmca) crystal structure, and a θ–2θ scan clearly demonstrates the preferred peaks corresponding to $[0\,k\,0]$ ($k = 2, 4, 6$) planes (figure 1(e)), revealing a highly oriented growth of BP. Only phosphorous element can be found in the energy dispersive x-ray spectroscopic elemental analysis (figure S1(b)), confirming the purity of the crystals.

The atomic structure of the BP crystal is resolved in figure 1(f) using high-resolution transmission electron microscopy (TEM) with the [0 1 0] zone axis, i.e. the TP direction. The orthogonal lattice structure is demonstrated, and the corresponding selected area electron diffraction pattern clearly shows the AC and ZZ planes (figure 1(g)), also confirming the high crystallization quality of our samples.

Thermal stability and crystallographic orientations identification

Before the thermoelectric measurements, we conduct the temperature-dependent Raman spectroscopy within 300–623 K to test the thermal stability of our BP crystals, as shown in figure 2(a). The spectrum at room temperature has three typical peaks, including one through-plane mode at 363 cm^{-1} (A_g^1) and two in-plane modes at 439 cm^{-1} (B_{2g}) and 467 cm^{-1} (A_g^2), which is consistent with the previous report [20]. The sharp Raman features with FWHM $<5\,cm^{-1}$ suggest the high quality of the as-grown crystals. All the three Raman modes follow a red-shift as the temperature increases, similar to the previous report within 77–673 K [41]. The variations in the Raman peak positions have a linear dependence on the changes in temperatures, as plotted in figure 2(b). The data can be fitted according to the equation of $\omega(T) = \omega_0 + \chi T$, where ω_0 is the extrapolated peak position at zero Kelvin and χ is the first-order temperature coefficient. The slope of the fitted straight line represents the value of χ, which are -0.018, -0.031 and $-0.032\,cm^{-1}\,K^{-1}$ for A_g^1, B_{2g} and A_g^2 mode, respectively. At the same time, FWHM for all the Raman modes gradually increase with the increasing temperature. The Raman peak shift and broaden are mainly contributed by the anharmonicity and the thermal expansion. *In situ* high-temperature powder XRD of BP crystals is also studied from 300 to 573 K (figure S2(a)), and the results show that the BP crystals remain crystalline within this temperature range. The downward shift of the peaks suggests a slight expansion of the BP unit-cell with the increasing temperature.

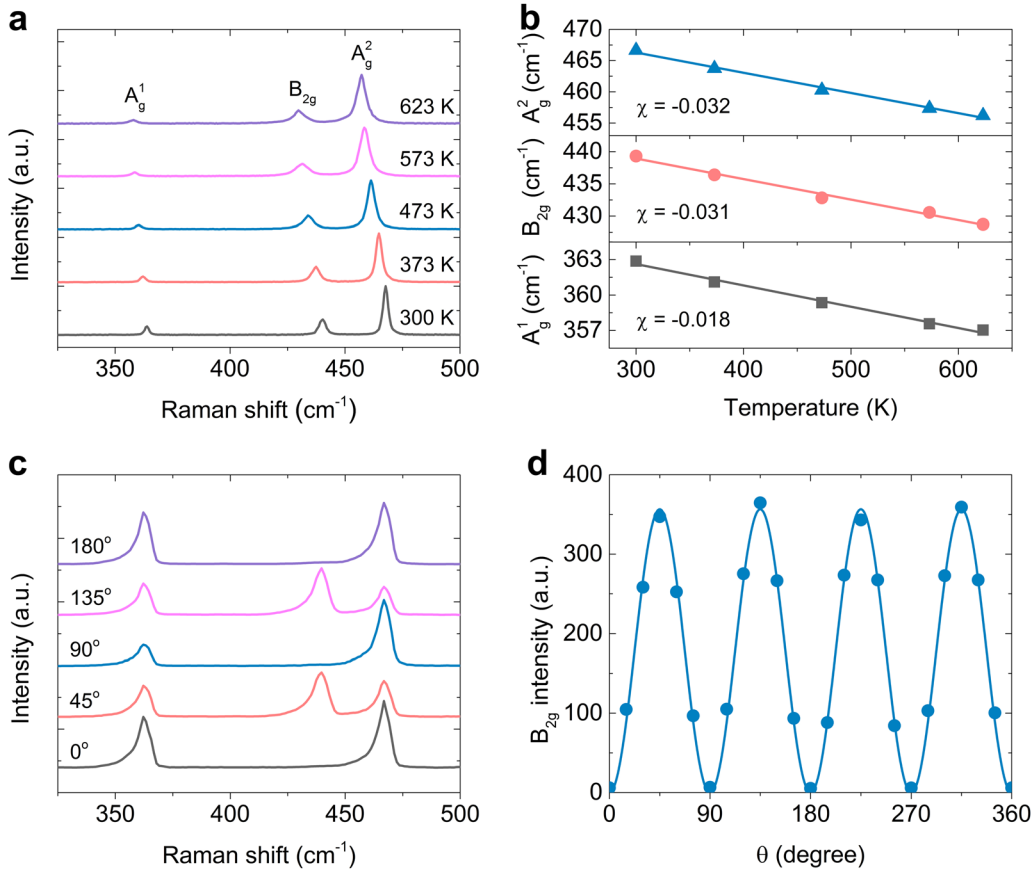

Figure 2. Temperature-dependent and angle-resolved polarized Raman spectroscopy. (a) Raman spectra from 300 K to 623 K for BP bulk crystal. (b) Temperature dependence of the variation for the three Raman modes, χ is the first-order temperature coefficient. (c) Typical angle-resolved polarized Raman spectra of BP crystal from 0° to 180°. The angle of 0° is defined at when excitation polarization is parallel to the ZZ direction. (d) Angle dependence of the intensity of the B_g^2 peak.

The crystalline orientations of BP crystals should also be identified before the anisotropy measurements. We conduct angle-resolved polarized Raman spectroscopy [20, 21] under parallel polarization configuration with the BP samples rotated by every 15° to determine the AC and ZZ directions. Representative angle-resolved polarized Raman spectra of BP samples from 0° to 180° with the multiples of 45° are exhibited in figure 2(c) (The angle of 0° is defined at when excitation polarization is parallel to the ZZ direction). The details of the polarization dependence for the A_g^1, B_{2g} and A_g^2 mode are showed in figures S2(b)–(d). The A_g^1 mode has a 180° variation period, and its intensity reaches the maximum and minimum values at 0°/180° and 90° respectively. The A_g^2 mode, on the other hand, has a 90° variation period, which reaches the maximum value at 0°/90°, and becomes much weaker at 45°. Furthermore, the intensity of the B_{2g} mode has a 90° variation period, which reaches the maximum value at around 45° and is completely forbidden at 0°/90°. Therefore, the intensity of the B_{2g} mode acts as an effective indicator of the crystal orientation [21], which can be fitted with a $\sin^2(2\theta)$ function, as shown in figure 2(d).

Thermoelectric measurements

The electrical conductivity and Seebeck coefficient were measured simultaneously in a helium atmosphere at 300–725 K using a ZEM-3 instrument system [42]. The Schematic of ZEM-3 setup and the optical image of our sample are shown in figure S3. The electrical conductivities for BP crystals along the AC and ZZ directions demonstrate the same temperature-dependent trend (see figure 3(a)), including the metallic transport behavior from 300 to 475 K, and the thermally activated semiconducting behavior from 475 to 725 K. The upturn above 475 K is attributed to the thermal excitation of carriers. It can be seen that the electrical conductivity along the AC direction (σ_{AC}) is higher than that along the ZZ direction (σ_{ZZ}), which are 64 and 36 S cm^{-1} respectively at 300 K, and the ratio of σ_{AC}/σ_{ZZ} is around 1.8 within the whole measurement temperature range. The σ_{ZZ} of BP bulk crystal at room temperature is in the same order as that of the exfoliated BP flake with a thickness of 75 nm (60 S cm^{-1}, figures S4(a) and (b)). The σ_{AC}/σ_{ZZ} ratio of BP bulk crystal is also close to the conductance ratio obtained by the angle-resolved DC conductance measurement on the exfoliated flake with a thickness of 110 nm (1.7, figures S4(c) and (d)), which is near to the values in previous reports [3, 5, 20]. At room temperature, our bulk crystals exhibit an order of magnitude higher electrical conductivity in both in-plane directions and almost a half lower σ_{AC}/σ_{ZZ} ratio than the ones in previous reports [1, 19]. The difference

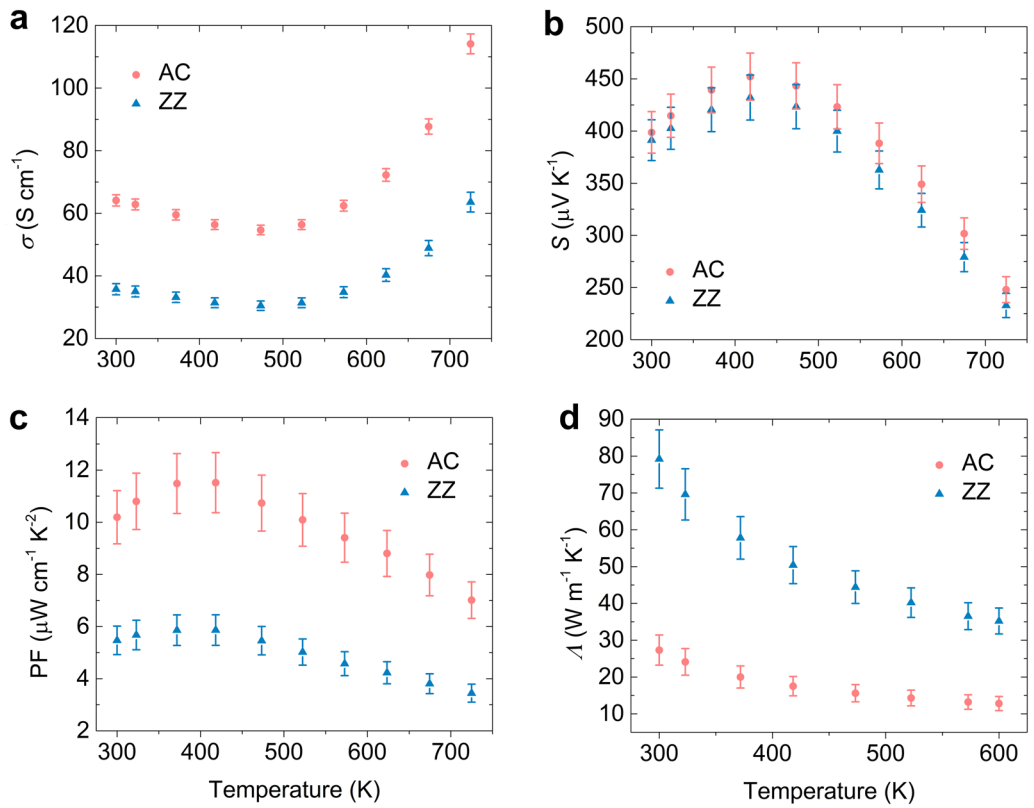

Figure 3. Thermoelectric properties along the AC and ZZ directions as a function of temperature for BP crystals. (a) Electrical conductivity. (b) Seebeck coefficient. (c) Power factor, PF. (d) Thermal conductivity. For ZEM-3 system, the uncertainty is 5% for the electrical conductivity and Seebeck coefficient, and is about 10% for power factor; for TDTR, the uncertainty is around 15% and 10% for the calculated thermal conductivity along the AC and ZZ direction, respectively.

should arise from the higher quality of our samples at the entire bulk crystal level because the values of our bulk crystals are close to the results obtained from the exfoliated flakes, which can be seen as perfect single crystals for such electrical measurements.

As exhibited in figure 3(b), the Seebeck coefficients display p-type properties due to the positive values, and show almost isotropic behavior along the AC and ZZ directions, which is consistent with the theoretical predictions [31, 43] and similar to that of the SnSe crystal [44]. The isotropic nature of the Seebeck coefficient would be ascribed to the uniform distribution of the carrier density [5] and the density of states in bulk BP crystals [43]. The Seebeck coefficients increase from 300 to 425 K and then decrease from 425 to 725 K, which is almost completely opposite to the temperature-dependent trend of the electrical conductivity. The Seebeck coefficient and the corresponding temperature-dependent behavior below 400 K agree with that reported on bulk poly-crystalline BP [45]. The maximum value of the Seebeck coefficient (S_{max}) is correlated to the bandgap (E_g) according to the equation of $E_g = 2eS_{max}T_{max}$ [46], where e is the electron charge and T_{max} is the critical temperature of S_{max}. Since the S_{max} is 452 μV K^{-1} along the AC direction and 432 μV K^{-1} along the ZZ direction at the T_{max} of 425 K, respectively, E_g for bulk BP can be estimated to be 0.37–0.38 eV, in consistent with the experimental result of 0.35 eV [6].

Due to the high Seebeck coefficient and moderate electrical conductivity, the power factor $PF = S^2\sigma$ along the AC direction achieves 10.2 μW cm^{-1} K^{-2} at 300 K, which gradually increases to the maximum of 11.5 μW cm^{-1} K^{-2} at 425 K, and then decreases to around 7 μW cm^{-1} K^{-2} at 725 K (figure 3(c)). These power factor values are comparable to those obtained for PbTe- and PbS-based thermoelectric materials in the same temperature range [47, 48]. The power factor along the ZZ direction is around a half of that along the AC direction, and the lower value mainly originates from the lower electrical conductivity.

We employ the conventional TDTR to measure the TP thermal conductivity (Λ_{TP}) [49, 50], and the beam-offset TDTR to measure the in-plane thermal conductivity of bulk BP along the AC (Λ_{AC}) and ZZ (Λ_{ZZ}) directions [18, 51]. More details of our TDTR measurements are described in our previous publication [18]. In the beam-offset method, we offset the probe beam along the AC and ZZ directions, which are predetermined from the polarized Raman spectroscopy. Since the heat diffusion along the beam-offset direction is mainly determined by the thermal conductivity along the corresponding direction, we can extract the in-plane thermal conductivity along this direction accurately. There could be a small angle between the beam-offset direction and the AC (or ZZ) direction as the determination of crystallographic orientations by polarized Raman spectroscopy is not perfect.

However, the slight deviation induced by the crystallographic orientations would hardly affect the accuracy of our thermal conductivity measurements as it is much smaller than the measurement uncertainty we calculated [18].

We find that the thermal conductivities of BP bulk crystals in all crystallographic orientations (Λ_{AC}, Λ_{ZZ}, Λ_{TP}) are inversely proportional to the temperature for the temperature range of 300–600 K (see figure S5), similar to what we found in our previous measurements of BP crystals at lower temperatures of 80–300 K [18]. The same T^{-1} temperature dependence for all Λ_{AC}, Λ_{ZZ}, Λ_{TP} suggests that phonons are scattered mainly by the same Umklapp process in BP irrespective of the crystallographic orientations. As a result of the same temperature dependence, we observe a constant anisotropy ratio in the thermal conductivities of $\Lambda_{ZZ}/\Lambda_{AC} \approx 2.8$, as shown in figure 3(d). Ranging from 300 to 600 K, Λ_{ZZ} varies from 80 W m^{-1} K^{-1} to 35.2 W m^{-1} K^{-1}, while Λ_{AC} varies from 28 W m^{-1} K^{-1} to 12.8 W m^{-1} K^{-1}. Similar anisotropy ratio has also been observed in previous low-temperature experiments [17, 18] and theoretical predictions [17, 18, 52, 53]. The structure-induced thermal transport anisotropy observed here is largely temperature independent because the same phonon–phonon scatterings dominate heat transport in all directions. This thermal transport anisotropy is fundamentally different from the temperature-dependent anisotropy induced by phonon-dislocation scatterings that we recently observed [54].

The combined higher power factor and lower thermal conductivity along the AC direction results in a much higher ZT value than that along the ZZ direction, and the ZT value in both the AC and ZZ direction (ZT_{AC} and ZT_{ZZ}) monotonically rises up along with the increasing temperature from 300 K to 600 K, as shown in figure 4. The room temperature ZT_{AC} and ZT_{ZZ} of our bulk BP crystals are 0.011 and 0.0021 respectively, which are around three times larger than that of the nanoribbons with a thickness of ~200 nm in previous report [14]. The larger values in this work could be more intrinsic due to the damage-free sample preparation and measurement processes. ZT_{AC} and ZT_{ZZ} reach the maximum values of 0.043 and 0.0075 at 600 K, respectively. ZT_{AC} is 5.4–5.7 times larger than ZT_{ZZ} within the whole measurement temperature range (see the inset in figure 4), exhibiting an outstanding anisotropic thermoelectric property.

Conclusion

In summary, we successfully synthesize big size and high-quality BP crystals via a chemical vapor transport method, and systematically study the in-plane anisotropic thermoelectric performances of such BP bulk crystals in the temperature range from 300 K to 600 K. The electrical conductivity and thermal conductivity demonstrate obvious opposite anisotropy between the AC and ZZ directions with a ratio of $\sigma_{AC}/\sigma_{ZZ} \approx 1.8$ and $\Lambda_{ZZ}/\Lambda_{AC} \approx 2.8$ respectively, while the Seebeck coefficient shows almost isotropic behavior. Therefore, the resulting ZT value along the AC direction is around 5.5 times of that along the ZZ direction, possessing significant in-plane anisotropy over the whole temperature range. These results reveal intrinsic, orientation-dependent thermoelectric performances of pristine BP crystals, which would not only serve as a baseline for the fundamental thermoelectric properties of BP, but also provide important design guidelines in device applications.

Methods

Powder XRD

The room temperature power XRD measurement was performed on a Bruker D8 powder XRD system with a Cu-Kα target, while the *in situ* temperature dependent XRD patterns were measured with a Siemens D5005 XRD System.

TEM characterization

The high-resolution TEM image and the selected area electron diffraction pattern were obtained under an accelerated voltage of 200 kV on a JEOL JEM-ARM300F transmission electron microscope with spherical aberration correctors.

Raman spectroscopy

All the Raman spectra were collected on a WITec Raman system with 532 nm incident laser. The laser power on the sample was kept below 1 mW to avoid damaging the sample. For polarization-dependent Raman experiments, a polarization analyzer was placed before the detector to form the parallel polarization configuration. For temperature dependent Raman measurements, a Linkam temperature controlled stage was used to set the measurement temperatures.

Electrical transport properties

The BP crystals were transferred and fixed on a glass substrate after the orientations were identified, and then were cut into regular stripes with the length of around 5 mm and the width of 1–1.5 mm, as shown in figure S3. The thickness of the samples was measured by a micrometer. The electrical conductivity and the Seebeck coefficient were simultaneous measured using a ZEM-3 instrument under a helium atmosphere from 300 K to 725 K. The uncertainty of the electrical conductivity and Seebeck coefficient measurements is 5%, and is about 10% for the power factor [44].

TDTR and beam-offset TDTR

TDTR and beam-offset TDTR measurements are similar to what we used in our previous report [18]. To prepare the BP samples for measurements, a 100 nm-thick Al film was deposited on the BP samples with a fresh surface. The Al film also protects the BP

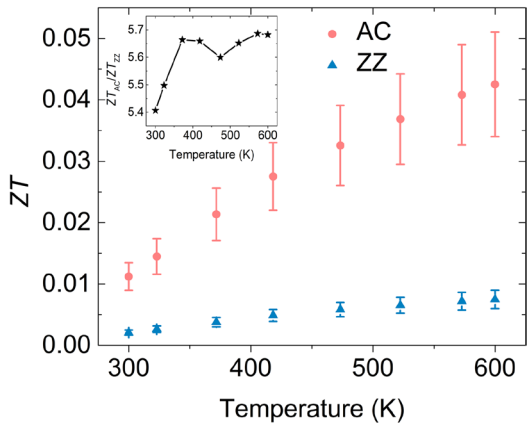

Figure 4. *ZT* values along the AC and ZZ directions from 300 to 600 K. Inset: the ratio of *ZT* values between the AC and ZZ direction (ZT_{AC}/ZT_{ZZ}). The ZT measurement uncertainty is about 20%.

surfaces from oxidation. In the conventional TDTR measurements, we employed a $1/e^2$ radius of 25 μm for the laser beams and a modulation frequency of 0.5 MHz, to ensure quasi-1D heat flow. In the beam-offset TDTR measurements, we instead employed a smaller laser $1/e^2$ radius of around 4 μm (and again a modulation frequency of 0.5 MHz), to create wide in-plane heat spreading. In the beam offset TDTR measurements, offset of pump and probe beams in either the ZZ or the AC directions leads to a convolution of the probe beam and the temperature profile created by pump beam at the sample surface. We then derived the in-plane thermal conductivity from FWHM of the beam-offset measurements by comparing FWHM with calculations of an anisotropic thermal model [51], as shown in the example at 420 K in figure S6. For more detailed explanations of our measurements, readers are referred to the experimental section and the supporting information of reference [18]. The calculated uncertainty has an upper limit of 15% for Λ_{AC} and 10% for Λ_{ZZ} at all temperatures, considering the uncertainties for all the parameters (e.g. heat capacity and density of BP) that we put in the thermal model [49, 51]. The combined uncertainty for all measurements involved in the calculation of *ZT* is around 20%.

Acknowledgments

This work is supported by the Singapore National Research Foundation under NRF award number MOE Tier 2 MOE2015-T2-2-007, MOE2015-T2-2-043 and MOE2016-T2-2-153.

ORCID iDs

Xun Cao https://orcid.org/0000-0002-6034-381X
Zexiang Shen https://orcid.org/0000-0001-7432-7936
Zheng Liu https://orcid.org/0000-0002-8825-7198

References

[1] Akahama Y, Endo S and Narita S 1983 *J. Phys. Soc. Japan* **52** 2148–55
[2] Li L K, Yu Y J, Ye G J, Ge Q Q, Ou X D, Wu H, Feng D L, Chen X H and Zhang Y B 2014 *Nat. Nanotechnol.* **9** 372–77
[3] Liu H, Neal A T, Zhu Z, Luo Z, Xu X F, Tomanek D and Ye P D 2014 *Acs Nano* **8** 4033–41
[4] Qiao J S, Kong X H, Hu Z X, Yang F and Ji W 2014 *Nat. Commun.* **5** 4457
[5] Xia F N, Wang H and Jia Y C 2014 *Nat. Commun.* **5** 4458
[6] Li L K *et al* 2017 *Nat. Nanotechnol.* **12** 21–5
[7] Brown A and Rundqvist S 1965 *Acta Crystallogr.* **19** 684–85
[8] Yuan H T *et al* 2015 *Nat. Nanotechnol.* **10** 707–13
[9] Wang X M, Jones A M, Seyler K L, Tran V, Jia Y C, Zhao H, Wang H, Yang L, Xu X D and Xia F N 2015 *Nat. Nanotechnol.* **10** 517–21
[10] Ling X *et al* 2016 *Nano Lett.* **16** 2260–7
[11] Mao N N *et al* 2016 *J. Am. Chem. Soc.* **138** 300–5
[12] Zhang G W, Huang S Y, Chaves A, Song C Y, Ozcelik V O, Low T and Yan H G 2017 *Nat. Commun.* **8** 14071
[13] Luo Z, Maassen J, Deng Y X, Du Y C, Garrelts R P, Lundstrom M S, Ye P D and Xu X F 2015 *Nat. Commun.* **6** 8572
[14] Lee S *et al* 2015 *Nat. Commun.* **6** 8573
[15] Jang H J, Wood J D, Ryder C R, Hersam M C and Cahill D G 2015 *Adv. Mater.* **27** 8017–22
[16] Zhu J *et al* 2016 *Adv. Electron. Mater.* **2** 1600040
[17] Smith B, Vermeersch B, Carrete J, Ou E, Kim J, Mingo N, Akinwande D and Shi L 2017 *Adv. Mater.* **29** 1603756
[18] Sun B, Gu X K, Zeng Q S, Huang X, Yan Y X, Liu Z, Yang R G and Koh Y K 2017 *Adv. Mater.* **29** 1603297
[19] Machida Y, Subedi A, Akiba K, Miyake A, Tokunaga M, Akahama Y, Izawa K and Behnia K 2018 *Sci. Adv.* **4** eaat3374
[20] Wu J X, Mao N N, Xie L M, Xu H and Zhang J 2015 *Angew. Chem., Int. Ed.* **54** 2366–9
[21] Kim J, Lee J U, Lee J, Park H J, Lee Z, Lee C and Cheong H 2015 *Nanoscale* **7** 18708–15
[22] Ling X, Liang L B, Huang S X, Puretzky A A, Geohegan D B, Sumpter B G, Kong J, Meunier V and Dresselhaus M S 2015 *Nano Lett.* **15** 4080–8
[23] Ribeiro H B, Pimenta M A, de Matos C J S, Moreira R L, Rodin A S, Zapata J D, de Souza E A T and Neto A H C 2015 *Acs Nano* **9** 4270–6
[24] Lu W L, Ma X M, Fei Z, Zhou J G, Zhang Z Y, Jin C H and Zhang Z 2015 *Appl. Phys. Lett.* **107** 021906
[25] Tao J *et al* 2015 *Acs Nano* **9** 11362–70
[26] Wang Z H and Feng P X L 2015 *2D Mater.* **2** 021001
[27] Wang Z H, Jia H, Zheng X Q, Yang R, Ye G J, Chen X H and Feng P X L 2016 *Nano Lett.* **16** 5394–400
[28] Hong T, Chamlagain B, Lin W Z, Chuang H J, Pan M H, Zhou Z X and Xu Y Q 2014 *Nanoscale* **6** 8978–83
[29] Wu J *et al* 2015 *Acs Nano* **9** 8070–7
[30] Chen X L *et al* 2017 *Nat. Commun.* **8** 1672
[31] Fei R X, Faghaninia A, Soklaski R, Yan J A, Lo C and Yang L 2014 *Nano Lett.* **14** 6393–9
[32] Zhang J, Liu H J, Cheng L, Wei J, Liang J H, Fan D D, Shi J, Tang X F and Zhang Q J 2014 *Sci. Rep.* **4** 6452
[33] Wang Y *et al* 2016 *Appl. Phys. Lett.* **108** 092102
[34] Monaco G, Falconi S, Crichton W A and Mezouar M 2003 *Phys. Rev. Lett.* **90** 255701
[35] Liu X, Wood J D, Chen K-S, Cho E and Hersam M C 2015 *J. Phys. Chem. Lett.* **6** 773–8
[36] Jiang P Q, Lindsay L, Huang X and Koh Y K 2018 *Phys. Rev.* B **97** 195308
[37] Jiang P Q, Lindsay L and Koh Y K 2016 *J. Appl. Phys.* **119** 245705
[38] Kopf M, Eckstein N, Pfister D, Grotz C, Kruger I, Greiwe M, Hansen T, Kohlmann H and Nilges T 2014 *J. Cryst. Growth* **405** 6–10
[39] Nilges T, Kersting M and Pfeifer T 2008 *J. Solid State Chem.* **181** 1707–11

[40] Zhao M, Qian H L, Niu X Y, Wang W, Guan L, Sha J and Wang Y W 2016 *Cryst. Growth Des.* **16** 1096–103
[41] Late D J 2015 *ACS Appl. Mater. Interfaces* **7** 5857–62
[42] Zhao W Y, Tan H T, Tan L P, Fan S F, Hng H H, Boey Y C F, Beloborodov I and Yan Q Y 2014 *ACS Appl. Mater. Interfaces* **6** 4940–6
[43] Saito Y, Iizuka T, Koretsune T, Arita R, Shimizu S and Iwasa Y 2016 *Nano Lett.* **16** 4819–24
[44] Zhao L D, Lo S H, Zhang Y S, Sun H, Tan G J, Uher C, Wolverton C, Dravid V P and Kanatzidis M G 2014 *Nature* **508** 373–7
[45] Flores E, Ares J R, Castellanos-Gomez A, Barawi M, Ferrer I J and Sanchez C 2015 *Appl. Phys. Lett.* **106** 022102
[46] Goldsmid H J and Sharp J W 1999 *J. Electron. Mater.* **28** 869–72
[47] Androulakis J, Lin C-H, Kong H-J, Uher C, Wu C-I, Hogan T, Cook B A, Caillat T, Paraskevopoulos K M and Kanatzidis M G 2007 *J. Am. Chem. Soc.* **129** 9780–8
[48] Johnsen S, He J Q, Androulakis J, Dravid V P, Todorov I, Chung D Y and Kanatzidis M G 2011 *J. Am. Chem. Soc.* **133** 3460–70
[49] Cahill D G 2004 *Rev. Sci. Instrum.* **75** 5119–22
[50] Sun B and Koh Y K 2016 *Rev. Sci. Instrum.* **87** 064901
[51] Feser J P, Liu J and Cahill D G 2014 *Rev. Sci. Instrum.* **85** 104903
[52] Zhu L Y, Zhang G and Li B W 2014 *Phys. Rev.* B **90** 214302
[53] Jain A and McGaughey A J H 2015 *Sci. Rep.* **5** 8501
[54] Sun B, Haunschild G, Polanco C, Ju J, Lindsay L, Koblmüller G and Koh Y K 2019 *Nat. Mater.* **18** 136–40